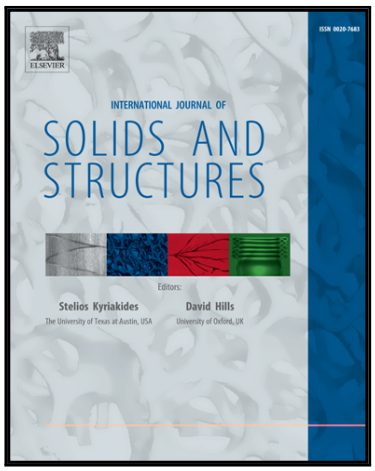

Experimental and modelling study of fatigue crack initiation in an aluminium beam with a hole under 4-point bending

Wenye Ye, Panos Efthymiadis, Christophe Pinna, Anxin Ma, Barbara Shollock, Richard Dashwood

PII: S0020-7683(18)30002-7
DOI: 10.1016/j.ijsolstr.2018.01.001
Reference: SAS 9850

To appear in: *International Journal of Solids and Structures*

Received date: 16 May 2017
Revised date: 30 October 2017
Accepted date: 4 January 2018

Please cite this article as: Wenye Ye, Panos Efthymiadis, Christophe Pinna, Anxin Ma, Barbara Shollock, Richard Dashwood, Experimental and modelling study of fatigue crack initiation in an aluminium beam with a hole under 4-point bending, *International Journal of Solids and Structures* (2018), doi: 10.1016/j.ijsolstr.2018.01.001

Experimental and modelling study of fatigue crack initiation in an aluminium beam with a hole under 4-point bending

Wenye Ye[a,b], Panos Efthymiadis[b], Christophe Pinna[c], Anxin Ma[a], Barbara Shollock[d], Richard Dashwood[e]

[a] *Interdisciplinary Centre for Advanced Materials Simulation, Ruhr-University Bochum, Universitätsstr. 90 a, 44789 Bochum, Germany*
[b] *Warwick Manufacturing Group, International Manufacturing Centre, University of Warwick, Coventry CV4 7AL, UK, previously in the Department of Mechanical Engineering, the University of She-ffield, Mappin Street, Sheffield S1 3JD, UK*
[c] *Department of Mechanical Engineering, The University of Sheffield, Mappin Street, Sheffield S1 3JD, UK*
[d] *Warwick Manufacturing Group, Warwick University, Coventry, CV4 7AL, UK*
[e] *Vice Chancellor's Office, Coventry University, Coventry, CV1 5FB, UK*

Abstract

Slip bands and crack initiations were investigated by in-situ experiments and nonlocal CPFEM simulations systematically. Experimental techniques including EBSD, digital image correlation (DIC) and SEM have been used to obtain consistent grain orientations, local strain, as well as slip bands and microcracks in the same area of the sample surface. The realistic microstructure based on EBSD map has been generated and used for finite element modelling. An advanced nonlocal crystal plasticity model, which considers the isotropic hardening and kinematic hardening of plastic strain gradient, has been adopted. The simulation results match experimental results well from many aspects. It was found that total strain and averaged slip on slip

Email address: P.Efthymiadis@warwick.ac.uk (Panos Efthymiadis)

systems, combined with accumulated slip on specific slip planes help predict the location and orientation of slip bands and microcrack initialization correctly. Furthermore, a fatigue indicating parameter based on competition between maximum slip and the total slip has been proposed to reproduce experimental results.

Keywords: A. crack initiation, A. slip band, B. crystal plasticity, 4-points bending test, fatigue indicating parameter

1. Introduction

The fatigue life of metallic materials usually goes through three main stages as crack initiation, crack propagation and failure. The microstructure features of the material determine the location sites for the appearance of cracks, which usually take place in these regions such as triple points, particle-matrix interfaces, pores and so called *weak* grains. Although crack initiation plays a dominant role in the whole process of fatigue, it has received relatively less attention than crack propagation. Nevertheless, many studies have been done in this field (e.g. (Christ et al., 2009) and (Sangid et al., 2011)). Various experiments have been conducted to observe how cracks formed in the material, and a large number of numerical models have been established to predict crack initiation in past decades.

A large number of experiments with different materials under different loading conditions have been conducted through the years to observe the micro-cracks. For example, Bozek et al. (2008) studied the fatigue process on double edge-notched (DEN) specimens. They observed cracks in most of Al_7Cu_2Fe particles only after the first fatigue cycle. The observations are

consistent with that of many others similar experiments reported in literature. Cheong et al. (2007) carried out a four-point bending fatigue test of an aluminum sample, which was subjected to high cycle fatigue (HCF) and the microstructure was characterized by EBSD analysis. Valuable investigation on crack initiation under uniform tensile stress has been carried out. Alexandre et al. (2004) and Findley (2005) showed that the crack initiation life depends on the relative sizes of the grains and inclusions. Alexandre et al. (2004) found that cracks formed only at slip bands for materials with large grain size. Jablonski (1981) found that crack initiation originated in persistent slip bands of a ceramic material, with these regions having more tendency to incubate cracks that those regions where the inclusion diameter was less than or equal to the grain size.

Many models have been proposed in the literature to predict crack incubation and growth. Tanaka and Mura (1981) assumed that crack initiation originates from slip bands, without consideration of cyclic hardening effect. Bozek et al. (2008) made a probabilistic simulation of constituent particle cracking in a specimen. They used a reduced number of particles to simulate crack initiation and micro-structurally small crack propagation. Hochhalter et al. (2010) adopted two slip-based metrics to study crack initiation, one based on the slip on the dominant slip systems and the other on the summation of slip on all slip systems. They found that the metrics and local stresses are crucial to predict crack initiation. Many studies (Fine and Bhat, 2007; Mura and Nakasone, 1990; Tanaka and Mura, 1981; Bobylev et al., 2010; Xie et al., 2016) proposed that an energy barrier must be overcome during fatigue crack initiation for forming new surfaces.

The combination of a representative volume element (RVE) and the crystal plasticity finite element method (CPFEM) is a powerful tool which could be used to evaluate crack initiation and propagation inside a computational micro-mechanics framework (Anahid and Ghosh, 2013; Bache et al., 2010; Brahme et al., 2011; Dunne et al., 2007; Kuhlmann-Wilsdorf, 1999; Li et al., 2012; Repetto and Ortiz, 1997; Robert et al., 2012; Bennett and McDowell, 2003; Sweeney et al., 2013; Hoshide and Kusuura, 1998; Olfe et al., 2000). Li et al. (2015) adopted the CPFEM and a RVE under cyclic loading to identify the weakest regions where cracks initiate and obtained a relationship between microstructure and an energy efficiency factor. Cheong et al. (2007) studied cracks inside a 4-point bending fatigue test specimen. Their model correctly predicted the crack initialization sites observed in the experiment. Based on the Tanaka-Mura model, Shenoy et al. (2007) investigated the fatigue life of a polycrystalline Ni-base superalloy with the help of fatigue-indication-parameters (FIPs) distribution. Using a Voronoi tessellation with 100 grains (Brückner-Foit and Huang, 2006) and the Tanaka-Mura model, (Brückner-Foit and Huang, 2006) studied the heterogeneous stress distribution and estimated the number of cycles to initiate cracks. Their approach was able to describe the whole process of crack fatigue life and revealed a relationship between crack initiation and the number of load cycles. Huang et al. (2007) extended the often used 2D model to a mesoscopic model close to 3D and found that, although the analysis became more complicated, results for crack density were quite similar to that from the 2D model. Full 3D models have also been developed in recent studies and showed the importance of using a 3D model in predicting the fatigue life. Navarro et al. (2014) compared the re-

sults of fatigue life estimation from 2D and 3D models. They concluded that the 3D model gave better results under certain conditions, but the 2D model also produced results similar to the experimental results. Manonukul and Dunne (2004) investigated the crack initiation in Ni-based alloy under high- and low-cycle fatigue considering grain morphology and crystallographic orientation. It was found that the persistent slip bands (PSBs) and accumulated plastic deformation are important mechanisms for crack initiation. Results also showed that crack initiation occurs at *weak* grains under both LCF and HCF. Cyclic plasticity is also important in predicting crack initiation. Several studies showed that the application of cyclic plasticity led to performant predictions(Dunne et al., 2007; Manonukul et al., 2005; Tsutsumi et al., 2010; Kartal et al., 2014), sometimes with better results than those obtained using accumulated plasticity for some materials. Till now there still exist challenges including: construction of proper microstructures of multiphase engineering materials for finite element modelling, development of physical principle based crystal plasticity models considering hardening of strain gradients, and finding the relation between damage and microcrack initialization with local stress and strain. The RVE generation methods in some studies (Becker and Panchanadeeswaran, 1995; Cheong et al., 2007; Weiland and Becker, 1999; Becker and Weiland, 2000; Bhattacharyya et al., 2001; Cheong and Busso, 2004; St-Pierre et al., 2008; Choi et al., 2013; Zhang et al., 2016) often include mapping EBSD data to a coarser regular finite mesh (Cheong et al., 2007) or generate a statistic type Voronoi tessellation considering grain size distribution (Kozaczek et al., 1995). Regular meshed RVEs of polycrystals therefore contains steps and corners along grain boundaries which are

physically unrealistic and inaccurate since the mechanical properties of grain boundaries are very much dependent on both local misorientations and the grain boundary plane's normal vector direction. Simulation results from this kind of RVEs have therefore limitations in their prediction of deformation and failure measured through in-situ experiments.

In this paper, crack initiation and slip bands were investigated by in-situ experiments and CPFEM simulations systematically. A Deben vertical bending equipment was used to conduct a 4-points bending test over the sample with a hole. Experimental techniques including EBSD, digital image correlation (DIC) and SEM have been used to study crystal orientations, local strain distributions and slip band and micro-crack, respectively. Subsequently, a quasi-2D finite element model (a 3D material model for microstructure with a thickness of one finite element) of a realistic microstructure, based on EBSD maps, has been generated for simulations adopting an advanced nonlocal crystal plasticity model (Ma and Hartmaier, 2014), which considers the isotropic hardening and kinematic hardening of plastic strain gradient. In our study, since damage and micro-cracks appear after the first loading cycle, as shown by experimental results reported in section 2, the accumulated plastic strain is therefore proposed as an important factor for damage and micro-crack initiation for the investigated material. Based on the simulation results, different FIPs were calculated and compared. Some individual grains and related slip systems were found to be responsible for crack initialization under cyclic loading.

2. Experiment

2.1. Material and Methods

The experiment was performed using an aluminium alloy Al2024 T4 received as a $50mm$ thick plate. Samples were machined at mid-thickness of the plate. The dimensions of the specimen are $50mm$ (length)$\times 7mm$ (width)$\times 4mm$ (thickness), with a $1mm$ hole drilled in the center. The corresponding geometry and bending schematic are shown in Fig.1. The sample was electropolished at the top surface, in a solution containing 30% Nitric acid and 70% Methanol.

EBSD measurements were carried out using a FEI-Sirion SEM, the magnified EBSD map is shown in Fig.1. After EBSD measurements, the samples were re-polished and then etched to reveal microstructural features such as grain boundaries, particles and inclusions. Cyclic fatigue tests were conducted using a Deben testing stage working inside a CamScan SEM with a cross head speed of $2mm/min$, a frequency of $0.5Hz$ and a strain value of approximately 0.01 for the 4 points vertical bending geometries shown in Fig.1.

Local displacement- and strain maps were obtained by means of DIC (Efthymiadis, 2015; Alharbi et al., 2015). The natural features of the microstructure were used to perform the correlation. Measurements were carried out for a flat un-tilted specimen. The microstructure was slightly over-etched to clearly reveal more microstructural features and to increase the contrast of the inclusions and precipitates. The procedure to quantify errors relative to DIC measurements carried out inside a SEM has been reported in Ghadbeigi et al. (2012). Errors for strain values reported in this work

are smaller than 0.03 for all images obtained throughout the test. At first the image of the undeformed sample was taken as a reference. Subsequently, consecutive images were obtained at minimum and maximum displacements of each cyclic loading up to 500 cycles. These images were correlated to the reference image to calculate strain maps.

The two yellow boxes on the EBSD map in Fig.1 show areas, covering approximately an area of $2.25mm \times 1.5mm$, observed during the in-situ test. The micrographs were analysed using the commercial DIC software, DaVIS 7.0, LAVision to compute the in-plane displacement field from which the strain values were calculated, as explained in (Alharbi et al., 2015). A sensitivity analysis was pursued relative to the interrogation window size. Instead of using a constant interrogation window defined by the number of pixels, a multi-pass procedure of four passes, two passes with 32×32 pixels and another two with 16×16 pixels was selected for all the experimental results presented in this work. This procedure allows for a progressive reduction of the interrogation window, in order to get accurate measurements of the strains at the grain level. The local strain accuracy is 0.07% with the global strain accuracy 0.0006%. The minimum detectable displacement is 7.8 microns.

Errors due to the SEM imaging system were considered. Errors due to electron beam drift were assessed and were in line with results reported in (Ghadbeigi et al., 2012), with a non-uniform distribution over the analysed area but with magnitudes less than 0.5% which were deemed negligible compared to values up to 75% reported in Fig.2.

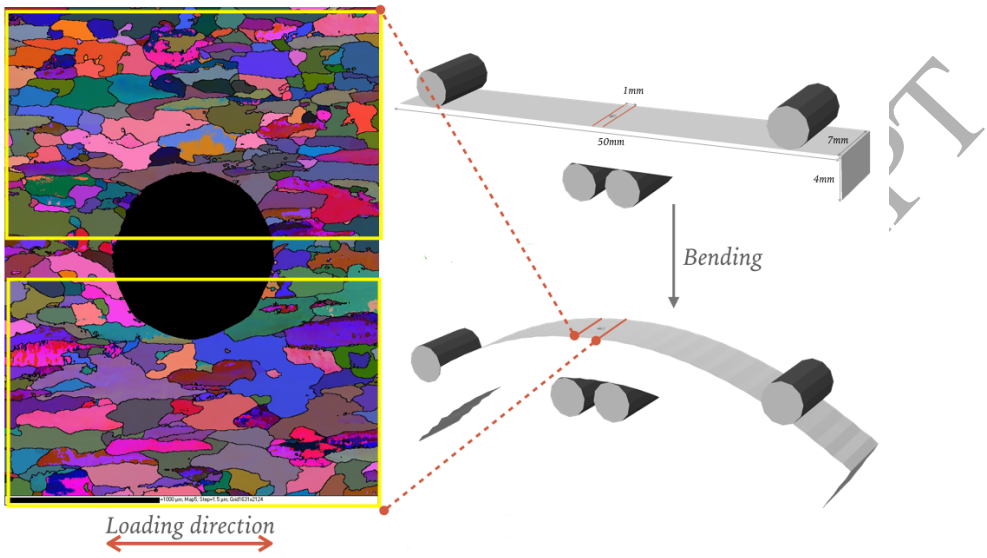

Figure 1: Schematic drawing of the 4-point bending test with two highlighted regions for EBSD and DIC investigation.

2.2. Experimental results

After the first bending cycle, micro-cracks were found in the two highlighted areas of the strain map (Fig. 2 (c) and (d)). The different microcrack locations infer that grain shape and grain orientation influence the crack initiation process strongly. As shown in Fig.2a, the DIC measured major strains are distributed highly non-uniformly over the microstructure. The highest strain magnitudes are observed in regions marked with white triangles near the edge of the central hole. Damage also occurred away from the hole edge in the upper triangle area. This suggests that strain magnitudes alone are not sufficient to predict crack initiation.

The higher magnification SEM images (Fig. 2b, c, d and e) show different crack-formation mechanisms on the sample surface. In one region (Fig. 2b, d), intense slip bands were observed after the first cycle with a crack initiated after 10 cycles along one slip band. Along the slip bands, microvoids have nucleated as shown in Fig.2c. Irreversible plastic slip and locally excessive plastic deformation are probably the main mechanisms leading to microvoid formation and microcracking along the formed slip bands.

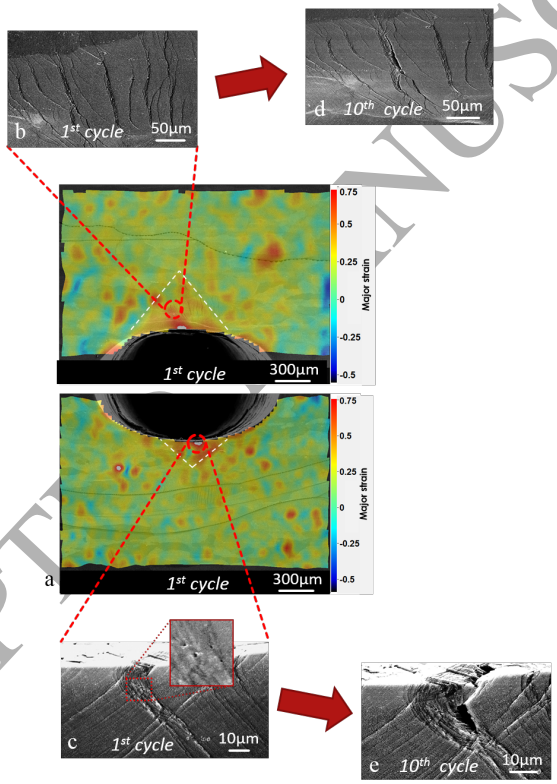

Figure 2: (a) Local tensile strain measured by DIC, (b), (c), (d), (e) slip bands and microcrack initiation observed in the SEM with microvoids highlighted in (c). The loading direction is horizontal in the images(Efthymiadis, 2015).

3. Simulation

3.1. Micro-structure for finite element modelling

In this study, the original EBSD map, shown in Fig.1, with some modification explained below has been used to generate a corresponding microstructure for FEM modelling. Large grains with their orientations and long grain boundaries were kept in the edited image. Some small grains were deleted. The original and edited images as well as the generated FEM mesh, directly created using Abaqus 6.11, can be seen in Fig.3. About 90% of the grains with the main features of the experimental microstructure have been captured perfectly. Due to the large grain size, it is expected that the influence of the subsurface grains is minimum. The model has a thickness of one finite element with plane strain conditions. The final microstructure contains 179 grains with different initial orientations. Due to the complex grain geometry, C3D4 (4-node linear tetrahedral) elements had to be used for the simulation. A total of 23,999 elements have been used to reproduce the details of the microstructure.

The displacements at the left and right edges of the DIC map were obtained and imported as boundary conditions into Abaqus. No significant alterations were observed for the displacement vectors at the two (left and right) edges of the DIC map in Fig. 2 during cyclic loading (up to the first 100 cycles).

3.2. The non-local crystal plasticity model

The CPFEM model was developed based on a large total deformation framework. Total deformation gradient $\mathbf{F}$ can be separated into elastic part

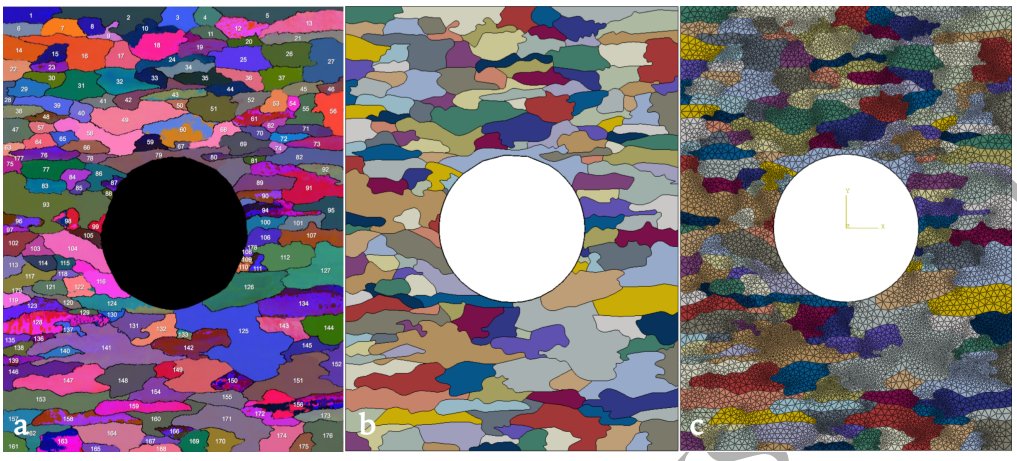

Figure 3: (a) Original microstructure, (b) simplified microstructure and (c) finite element mesh.

$\mathbf{F}^{\mathrm{e}}$ and plastic part $\mathbf{F}^{\mathrm{p}}$ by adopting the multiplicative decomposition approach (Lee, 1969).

$$\mathbf{F} = \mathbf{F}^{\mathrm{e}}\mathbf{F}^{\mathrm{p}} \ . \tag{1}$$

Elastic law (Hooke's law) can be defined in the intermediate configuration with the help of the stiffness tensor $\mathbb{C}$ and right Cauchy-Green tensor $\mathrm{C}_e = \mathbf{F}^{\mathrm{e}\mathrm{T}}\mathbf{F}^{\mathrm{e}}$ as

$$\widetilde{\mathbf{S}} = \frac{1}{2}\mathbb{C} : \left(\mathbf{F}^{\mathrm{e}\mathrm{T}}\mathbf{F}^{\mathrm{e}} - \mathbf{I}\right) \ , \tag{2}$$

where $\widetilde{\mathbf{S}}$ is the second Piola-Kirchhoff stress defined in the intermediate configuration.

Dislocation slip is the only mechanism considered for the plastic deformation, where dislocations glide on well defined slip systems. This widely used constitutive assumption (Asaro and Needleman, 1985; Kalidindi et al., 1992) is adopted for crystal plasticity. For the large deformation framework, if the initial plastic deformation gradient $\mathbf{F}^{\mathrm{p}0}$ and a small time increment are

given, plastic deformation gradient rate can be approximated as

$$\dot{\mathbf{F}}^{\mathrm{p}} = \sum_{\alpha=1}^{12} \dot{\gamma}_{\alpha} \widetilde{\mathbf{M}}_{\alpha} \mathbf{F}^{\mathrm{p0}} \ , \tag{3}$$

where $\dot{\gamma}_{\alpha}$ and $\widetilde{\mathbf{M}}_{\alpha}$ are the shear rate and the Schmid tensor for slip system α, respectively. The list of Schmid tensors of the FCC crystal structure is given in Table 1.

The following flow rule (for each slip system) is used in this study based on (Ma and Hartmaier, 2014), which incorporates the effect of the non-local hardening terms $\tau_{\alpha}^{\mathrm{GNDk}}$, $\hat{\tau}_{\alpha}^{\mathrm{GNDi}}$.

$$\dot{\gamma}_{\alpha} = \dot{\gamma}_0 \left| \frac{\tau_{\alpha} + \tau_{\alpha}^{\mathrm{GNDk}}}{\hat{\tau}_{\alpha}^{\mathrm{c}} + \hat{\tau}_{\alpha}^{\mathrm{GNDi}}} \right|^{p_1} \mathrm{sign}(\tau_{\alpha} + \tau_{\alpha}^{\mathrm{GNDk}}) \ . \tag{4}$$

In this equation, τ_{α} is the corresponding resolved shear stress of the slip system α, $\hat{\tau}_{\alpha}^{\mathrm{c}}$ represents the strain hardening term. $\hat{\tau}_{\alpha}^{\mathrm{GNDi}}$ is the isotropic hardening due to first order of plastic strain gradients and $\tau_{\alpha}^{\mathrm{GNDk}}$ is the kinematic hardening due to second order plastic strain gradients on slip system α. p_1 is the inverse value of the strain rate sensitivity. For a small elastic deformation, the resolved shear stress τ can be approximated as

$$\tau_{\alpha} = \widetilde{\mathbf{S}} \cdot \widetilde{\mathbf{M}}_{\alpha} \ . \tag{5}$$

Typical strain hardening caused by the accumulation of statistically stored dislocations (SSDs) for slip system α can be defined as

$$\dot{\hat{\tau}}_{\alpha}^{\mathrm{c}} = \sum_{\beta=1}^{12} h_0 \chi_{\alpha\beta} \left(1 - \frac{\hat{\tau}_{\beta}^{\mathrm{c}}}{\hat{\tau}^{\mathrm{sat}}} \right)^{p_2} |\dot{\gamma}_{\beta}| \ , \tag{6}$$

where $\dot{\gamma}_0$ is the reference shear rate, p_1 is the inverse value of the strain rate sensitivity, h_0 is the initial hardening rate, $\chi_{\alpha\beta}$ is the cross hardening matrix, $\hat{\tau}^{\mathrm{sat}}$ is the saturation slip resistance, and p_2 is a fitting parameter.

According to the currently used higher order non-local model (Ma and Hartmaier, 2014), the dislocation density tensor (Nye, 1953; Dai and Parks, 1997) obtained from the first gradient of $\mathbf{F}^{\mathrm{p}}$ can be rationalized to 9 super GND components. To evaluate the higher order stresses, gradients of super GND tensor are approximated as 27 super GND segments localized at specific position. Following the above approach, isotropic and kinematic hardening due to the first and second order gradients of plastic deformation ($\mathbf{F}^{\mathrm{p}}$) are calculated for slip system α.

$$\hat{\tau}_{\alpha}^{\mathrm{GNDi}} = c^{\mathrm{pass}} \mu b \sqrt{\sum_{\beta=1}^{9} \chi'_{\alpha\beta} \left| A_{\beta ij} \delta_{jkl} \left(\mathbf{F}^{\mathrm{p}} \otimes \boldsymbol{\nabla} \right)_{ikl} \right| / b} \ , \tag{7}$$

$$\tau_{\alpha}^{\mathrm{GNDk}} = \mathbf{F}^{\mathrm{p}} \mathbb{C}' \left(\mathbf{F}^{\mathrm{p}} \otimes \boldsymbol{\nabla} \otimes \boldsymbol{\nabla} \right) \mathbf{F}^{\mathrm{p}\mathrm{T}} \cdot \widetilde{\mathbf{M}}_{\alpha} \ . \tag{8}$$

In Eq. (7), the coefficient c^{pass} is used to calculate the passing stress of crystallographic mobile dislocations due to super GNDs as forest dislocation. Whereas μ, b, $\chi'_{\alpha\beta}$ are model parameters representing shear modulus, Burger vector (magnitude) and interaction matrix between crystallographic mobile dislocations and super GNDs, respectively. Apart from this, δ_{jkl} and $A_{\beta ij}$ in Eq. (7) are the third rank permutation tensor and third order conversion tensor and are used to evaluate the plastic strain gradients. Except for $A_{111} = A_{222} = A_{333} = A_{412} = A_{513} = A_{623} = A_{721} = A_{831} = A_{932} = 1$, the rest of the 72 components of $A_{\beta ij}$ are zero. The sixth order tensor $\mathbb{C}'$ in Eq. (8) depends on the stiffness tensor $\mathbb{C}$ and the average GND pile-up size L. One can refer to the detailed description of non-local terms in Ma and Hartmaier (2014).

The list of model parameters is given in Table 2. Values were reported in Luo and Chattopadhyay (2011), Luo (2011) and Efthymiadis (2015). These

parameters were calibrated from simple monotonic tensile tests as well as fully reversed cyclic tests.

Table 1: Schmid tensors of the FCC crystal structure

α	$\widetilde{\mathbf{M}}_\alpha = \widetilde{\mathbf{d}}_\alpha \otimes \widetilde{\mathbf{n}}_\alpha$	α	$\widetilde{\mathbf{M}}_\alpha = \widetilde{\mathbf{d}}_\alpha \otimes \widetilde{\mathbf{n}}_\alpha$
1	$(01\bar{1}) \otimes [111]/\sqrt{6}$	7	$(011) \otimes [1\bar{1}1]/\sqrt{6}$
2	$(10\bar{1}) \otimes [111]/\sqrt{6}$	8	$(10\bar{1}) \otimes [1\bar{1}1]/\sqrt{6}$
3	$(1\bar{1}0) \otimes [111]/\sqrt{6}$	9	$(110) \otimes [1\bar{1}1]/\sqrt{6}$
4	$(\bar{1}11) \otimes [\bar{1}11]/\sqrt{6}$	10	$(011) \otimes [11\bar{1}]/\sqrt{6}$
5	$(101) \otimes [\bar{1}11]/\sqrt{6}$	11	$(101) \otimes [11\bar{1}]/\sqrt{6}$
6	$(110) \otimes [\bar{1}11]/\sqrt{6}$	12	$(1\bar{1}0) \otimes [11\bar{1}]/\sqrt{6}$

3.3. Simulation results

3.3.1. Strain distributions

The strain gradients which produce isotropic and kinematic hardening strongly depend on grain size and hole size. In order to investigate the nonlocal hardening, the maximum principal strain distribution for simulations with and without nonlocal hardening are compared in Fig.4 and Fig.5. One can easily see that the nonlocal hardening of strain gradients only influence some details of the strain distribution as the grain size and hole size are rather large. From Fig.5, GND hardening, only found in the nonlocal model, is more extensively distributed throughout the microstructure, but with a lower magnitude compared to that of strain hardening in the nonlocal model. The strain magnitude and heterogeneity in Fig.5 is higher than that in the experiment. This is likely due to the small area of the microstructure

Table 2: Nonlocal crystal plasticity model parameters.

parameter	notation	value
elastic constant	c_{11}	112GPa
elastic constant	c_{12}	59.5GPa
elastic constant	c_{44}	24.7GPa
shear moduli	μ	48GPa
Poisson ratio	ν	0.3
reference shear rate	$\dot{\gamma}_0$	0.001
inverse of strain rate sensitivity	p_1	20
initial critical resolved shear stress	$\hat{\tau}_0$	82.5MPa
initial hardening rate	h_0	37MPa
saturating critical resolved shear stress	$\hat{\tau}_f$	100MPa
exponent of strain hardening	p_2	2.25
cross hardening coefficient	$\chi_{\alpha\beta}$	1.0
cross hardening coefficient for GND	$\chi_{\alpha\beta}^{\mathrm{GND}}$	1.0
geometrical factor	c_1	0.1
average dislocation pile-up size	L	8×10^{-7} m

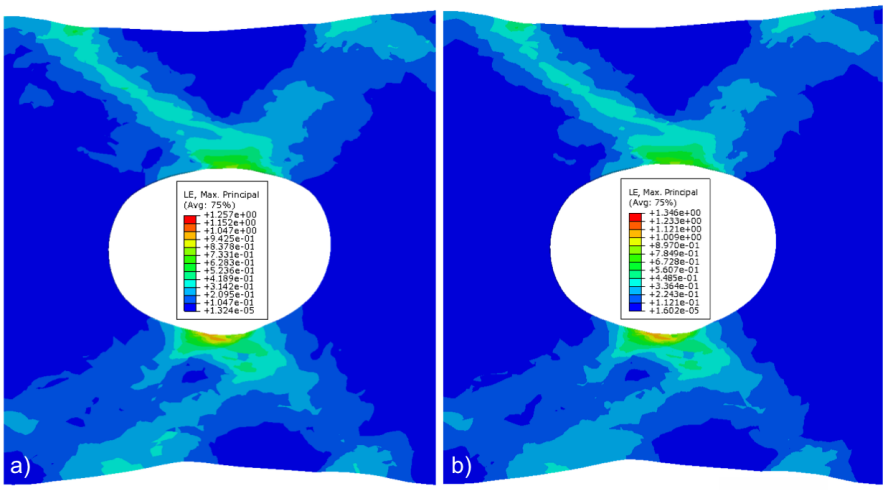

Figure 4: Maximum principal strain distributions by using a nonlocal model (a) and a local model (b).

simulated around the hole with the nodes in the upper and lower boundaries treated as free nodes in the simulation. The simulation results from the local model and the nonlocal model adopted the same model parameters listed in Table 2. The difference in terms of strain distribution is small, but the strain magnitude in the local model is slightly higher than that in the non-local model. This is quite reasonable as the local model is softer than the nonlocal model. Considering the high resemblance of local and nonlocal simulation results, in the following part of this paper, only results of the nonlocal model are reported.

The comparison between total strain and averaged slip on slip systems is given in Fig. 6. The total strain is the von-Mises strain. The accumulated slip is the time integration of the absolute shear rate on slip systems. The averaged slip is the average of accumulated strain of 12 slip systems. Grain

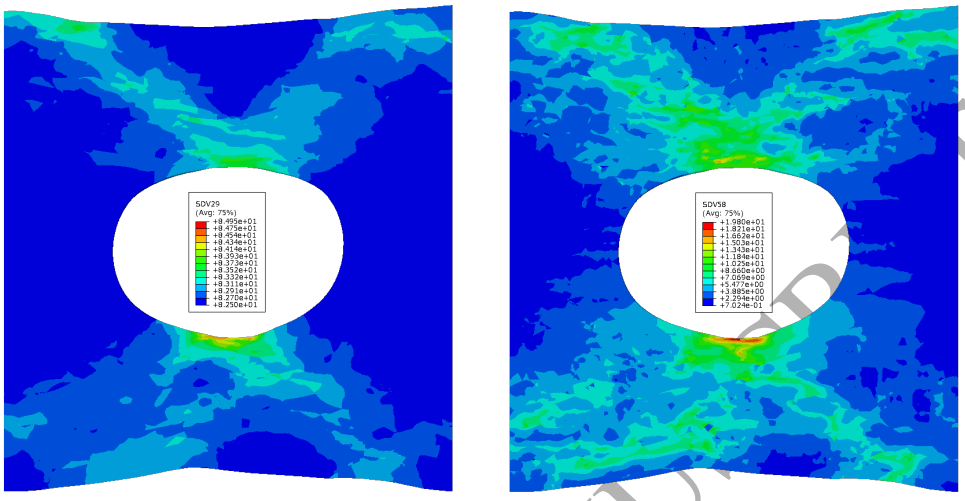

(a) (b)

Figure 5: Hardening distributions in (a) a nonlocal model with strain hardening (SVD29) and (b) a nonlocal model with GND hardening (SDV58).

boundaries, grain number, larger deformation regions as well as grains where microcracks were observed in the experiments are highlighted in the undeformed configuration. The strain distributions are rather heterogeneous. Although the strain field measured by DIC (Fig. 2b) does not show dominating deformation localization bands, a pronounced typical continuous 45° strain localization band at 45° with respect to the tensile direction and a partially continuous 45° plastic strain localization band, in the upper-left part of the sample, is predicted in the simulation. This is due to the simplified boundary conditions adopted in the simulation. The good agreement between strain distributions in the experiment and simulation appears in the regions near to upper-middle and lower-middle edges of the hole. The whole of grain-60

and part of grain-149 are inside these high strain regions. Since grain-125, for which slip bands and microcrack initiation were observed experimentally, does not fall in the high strain regions, total strain and averaged slip alone are not sufficient to predict fatigue crack initiation.

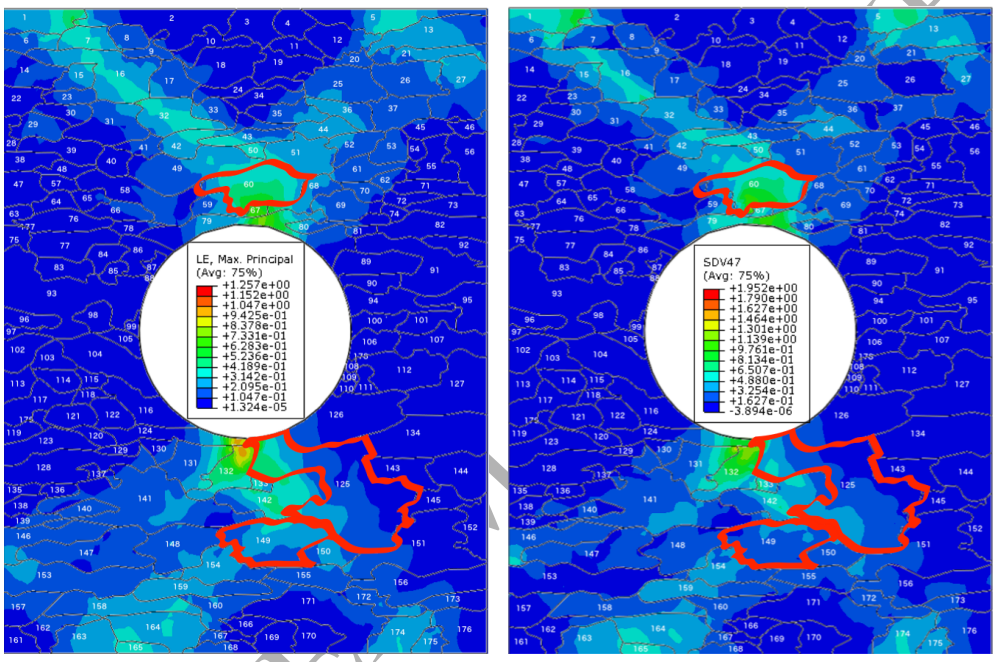

(a) (b)

Figure 6: Distribution of (a) total strain and (b) averaged slip on slip systems (SDV47) in undeformed configuration with grain numbers. Regions having large deformation and grains showing microcrack initiation have been highlighted.

3.3.2. Accumulated slip on slip systems

In order to explain different slip band and microcrack initialization mechanisms in different grains, the accumulated slip on each of the 12 slip systems has been calculated. As shown in Fig.6 and Fig.7, although the averaged slip

inside grain-125 is very low, the accumulated slip on the $(111)[0\bar{1}1]$ slip system is much higher than on other slip systems. Compared to the strong slip gradients on slip system $(\bar{1}11)[110]$ in grain-60 and on $(11\bar{1})[101]$ in grain-149, the slip in grain-125 is much more uniform. For this reason, according to Equation (8) grain-60 and grain-149 withstand higher kinematic hardening than grain-125.

Furthermore, with the help of Euler angles in the current configuration, the slip plane normal directions, the slip directions, and the intersection line directions of the slip plane with the sample surface with respect to the dominating slip systems in grain-60, grain-125 and grain-149 have been determined. These lines and directions are superimposed to the experimental image of the microstructure in Fig.8. The results in the deformed configuration show that the slip planes of slip systems 1, 5 and 10 have different angles with respect to y-direction. These angles, 68.13°, 90.72°and 78.76°, respectively, are in good agreement with experimental results. Through plotting FEM simulated values at gauss points using the software OVITO, the accumulated slip on four different slip planes was also compared. For example, the combination of slip on 10-11-12 slip systems (Fig.9d) supports the appearance of slip bands in the three important grains compared to results obtained for the three other cases (Fig.9a-9c). These simulations results therefore give some useful insight into the formation of slip bands observed in the SEM images.

3.4. Comparisons of different fatigue indicating parameters

Many fatigue indicating parameters (FIPs) have been proposed in the literature to predict crack initiation (Bozek et al., 2008; Shenoy et al., 2007;

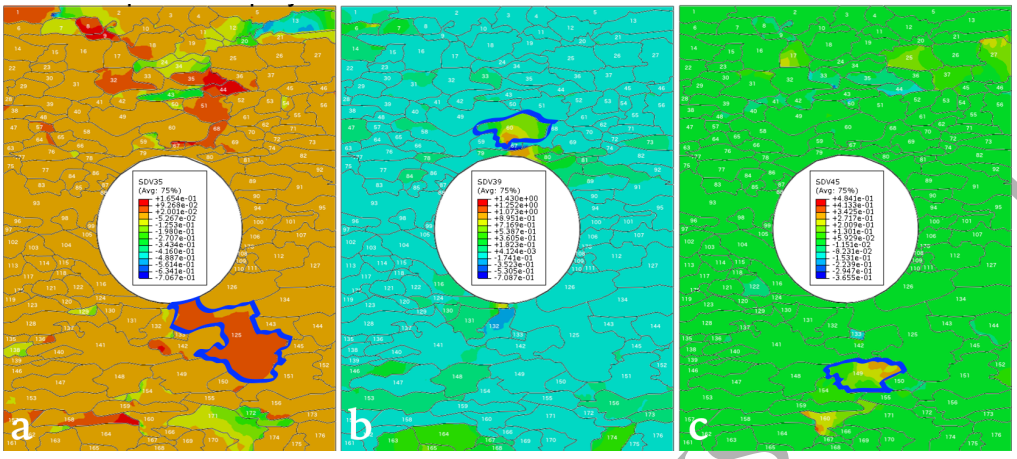

Figure 7: Accumulated slip on (a) slip system (111)[01$\bar{1}$] (SDV35), in (b) ($\bar{1}$11)[110] (SDV39)and (c) (11$\bar{1}$)[101] (SDV45) in c).

Manonukul and Dunne, 2004; Sweeney et al., 2013; Zhang and Jiang, 2006; Przybyla and McDowell, 2010). Very few publications have focused on comparing these parameters. The Fatemi-Socie (FS) parameter was selected in this study and was calculated inside the Abaqus UMAT subroutine. The FS parameter is defined as:

$$FS = \frac{\Delta\gamma_{max}}{2}\left(1 + k\frac{\sigma_n^{max}}{\sigma_y}\right) \tag{9}$$

where $\Delta\gamma_{max}$ is the maximum range of cyclic plastic shear strain, σ_n^{max} is the peak tensile stress normal to the plane which is associated with maximum shear range, σ_y is the yield strength and k is a constant that is fitted from the uniaxial and torsion fatigue test data.

When $k = 0$, it means that the crack incubation is independent of the normal stress and completely controlled by the irreversible motion of dislocations, in that case FS_{mps} only relates to the maximum range of cyclic plastic

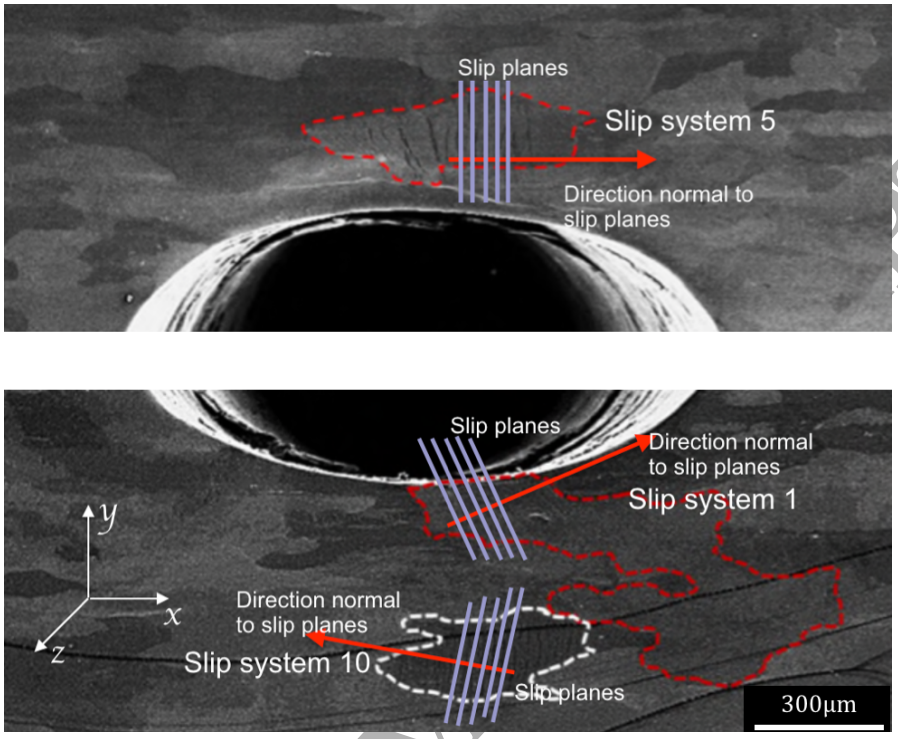

Figure 8: Comparison between simulated and measured slip band direction.

shear strain and amounts to:

$$FS_{mps} = \frac{\Delta\gamma_{max}}{2}. \tag{10}$$

Although the Fatemi-Socie parameter is traditionally used in macroscopic models of fatigue, it has more recently been introduced for the prediction of FCI and FCP (fatigue crack propagation) at the crystallographic level(Shenoy et al., 2007; Hochhalter et al., 2010, 2011). This parameter therefore depends on the maximal shear strain magnitude variation and the normal stress acting on slip planes. The amount of shear on each slip system was compared at the beginning and at the end of each load cycle to find the

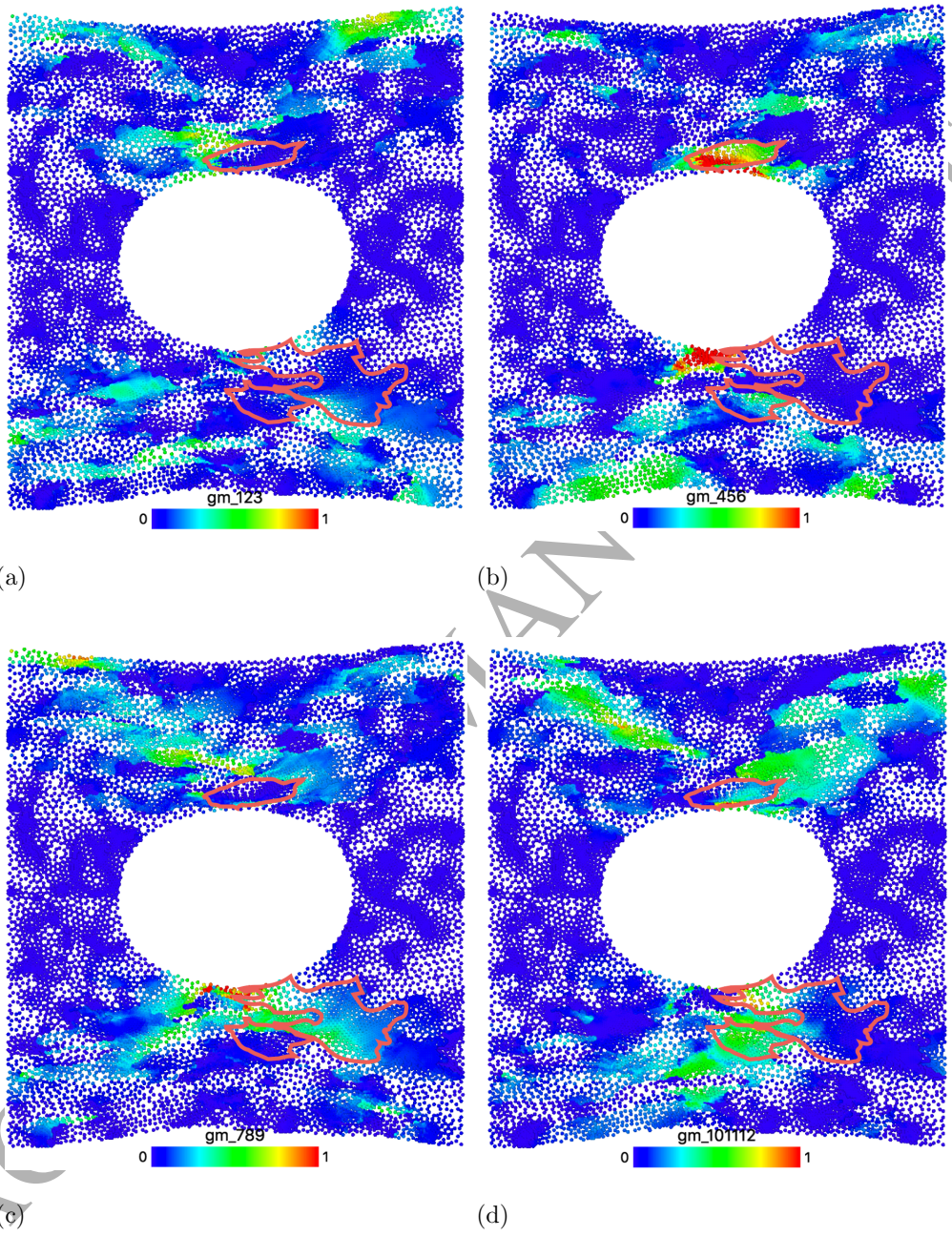

Figure 9: Distribution of accumulated slips on (a) (111) plane, (b) ($\bar{1}11$) plane, (c) ($1\bar{1}1$) plane, (d) ($11\bar{1}$) plane.

magnitude of maximal shear variation along with the normal stresses. As the maximal shear is assumed to cause a cleavage type micro-crack parallel to a slip plane, the normal stress on this slip plane is related to the growth of the crack at the microstructural scale.

Fig.10 shows the FS distribution map, with the value of constant k set to 1.2, for both monotonic and cyclic conditions. This parameter does predict correctly crack initiation at the red arrowed locations of Fig.10. Both locations correspond to the very edge of the hole where crack initiation occurred. There is a slight shift with respect to the location for crack initiation between Fig.10a and b, moving from monotonic to cyclic loading conditions. The location is better predicted when used cyclic loading conditions in the simulation. However, at the black-arrowed locations, crack initiation is not predicted correctly, as in the simulation (both for monotonic and cyclic) failure occurs at the edge of the hole, while in the experiment it occurs at a distance from the hole. As a result a new FIP parameter is proposed, which consists of two sub-parameters

$$D^* = \sqrt[(2\alpha+\beta)]{D_1^{2\alpha} \cdot D_3^{\beta}} \tag{11}$$

where D_1 represents the maximum accumulated slip system, and D_3 represents the total accumulated slip over all slip systems (Bozek et al., 2008).

For this study $\alpha = \beta = 1$. The reason for choosing a larger exponent for D_1 is that the maximum slip leads to the formation of strong slip bands and initiation of cracks. The exponent for D_3 is selected by considering that slip bands also formed outside critically loaded areas but they did not lead to fatigue crack initiation eventually. $(2\alpha + \beta)$ has been used in order to obtain dimensional consistency. Fig.11 shows simulation results when using

parameter D^*, with highly damaged areas predicted above and below the central hole. The map shows that crack initiation not only happens along the edge of the hole (red arrows), but also in other locations, close to the edge of the hole as pointed by black arrows. The locations predicted to fail do not change significantly between monotonic and cyclic loading conditions. The effect of grain orientation is more pronounced under cyclic loading conditions in Fig.11b. A shear band forms at the red-arrowed location close to the grain boundary of the highlighted grain. This indicates also the advantage of using a non-local CPFE model for predicting behaviours such as shear localisations within grains and strain localisations close to grain boundaries. By comparing Fig.2, Fig.10 and Fig.11, D^* predicts better the locations where fatigue crack initiation occurs under high amplitude cyclic loading conditions in comparison to the FS parameter. The sub-parameters D_1 and D_3 are both important factors for the prediction of the right locations for fatigue crack nucleation in the microstructure. These results therefore indicate that the Fatemi-Socie parameter is not as effective as the D^* parameter for predicting FCI for the investigated material but is a better predictor for modelling slow crack growth (SCG), as fatigue cracks always initiate along strong slip bands, but tend to deflect towards other directions upon SCG(Shenoy et al., 2007). However further validation of the proposed new criterion through experiments and simulations will be needed in the future.

4. Conclusion

In this paper, slip bands and crack initiation sites at the scale of the microstructure were investigated under cyclic loading using in-situ experiments

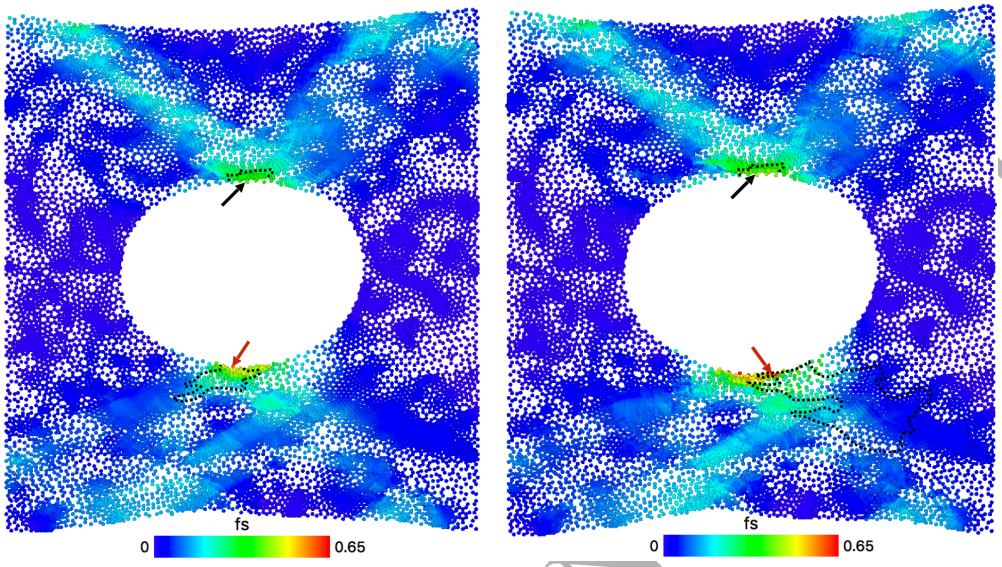

(a) (b)

Figure 10: Comparison of damage predictions by using parameter FS in monotonic (a) and cyclic (3 cycles) (b) loading conditions.

and CPFEM simulations systematically. Experimental techniques including EBSD, digital image correlation (DIC) and SEM were used to measure grain orientations, as well as local strain, distributions, and to analyse slip bands and microcrack formation in the same area of the sample surface. A realistic microstructure based on the EBSD map was generated and used for finite element modelling. An advanced nonlocal crystal plasticity model, which considers the isotropic hardening and kinematic hardening of plastic strain gradient, has been adopted. The simulation results are in good agreement with experimental results from many aspects:

1. It was found that some individual grains and related slip systems were

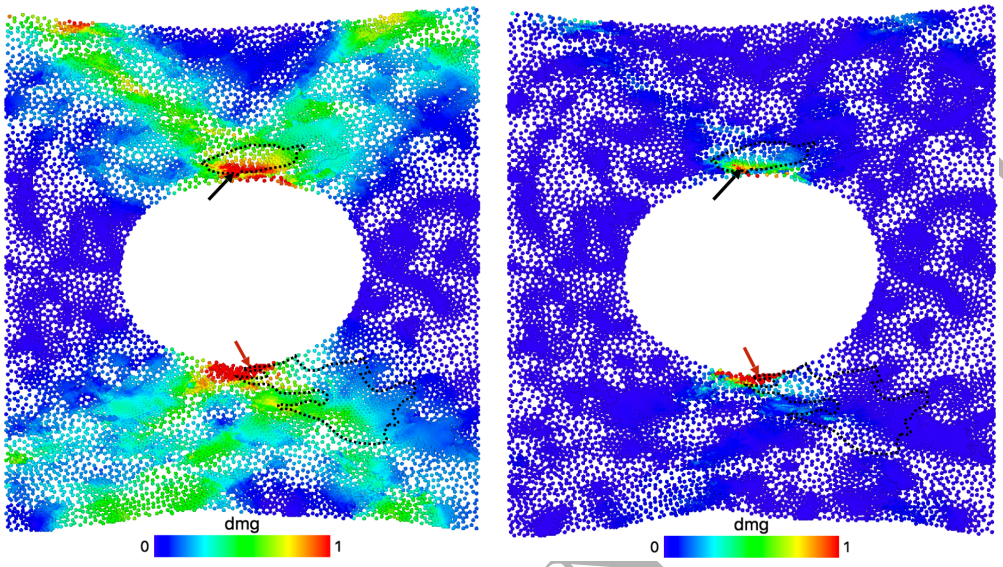

(a) (b)

Figure 11: Comparison of damage predictions by using parameter D^* in monotonic (a) and cyclic (3 cycles) (b) loading conditions.

responsible for crack initiation under cyclic loading.

2. Total strain and averaged slip on slip systems, combined with accumulated slip on specific slip planes correctly predict the location and orientation of slip bands as well as microcrack initiation sites.
3. A new fatigue indicating parameter based on the competition between maximum slip and total slip has been proposed and can reproduce experimental results.

Acknowledgements

The authors are grateful for the financial support provided by EPSRC under the grant EP/F023464/1.

References

References

Alexandre, F., Deyber, S., Pineau, A., 2004. Modelling the optimum grain size on the low cycle fatigue life of a ni based superalloy in the presence of two possible crack initiation sites. Scripta Materialia 50, 25–30.

Alharbi, K., Ghadbeigi, H., Efthymiadis, P., Zanganeh, M., Celotto, S., Dashwood, R., Pinna, C., 2015. Damage in dual phase steel dp1000 investigated using digital image correlation and microstructure simulation. Modelling & Simulation in Materials Science & Engineering 23, 085005.

Anahid, M., Ghosh, S., 2013. Homogenized constitutive and fatigue nucleation models from crystal plasticity fe simulations of ti alloys, part 2: Macroscopic probabilistic crack nucleation model. International Journal of Plasticity 48, 111–124.

Asaro, R., Needleman, A., 1985. Texture development and strain hardening in rate dependent polycrystals. Acta Metallurgica 33, 923–953.

Bache, M., Dunne, F., Madrigal, C., 2010. Experimental and crystal plasticity studies of deformation and crack nucleation in a titanium alloy. The Journal of Strain Analysis for Engineering Design 45, 391–399.

Becker, R., Panchanadeeswaran, S., 1995. Effects of grain interactions on deformation and local texture in polycrystals. Acta metallurgica et materialia 43, 2701–2719.

Becker, R., Weiland, H., 2000. Use of ebsd data in mesoscale numerical analyses, in: Electron Backscatter Diffraction in Materials Science. Springer, pp. 181–198.

Bennett, V., McDowell, D., 2003. Polycrystal orientation distribution effects on microslip in high cycle fatigue. International Journal of Fatigue 25, 27–39.

Bhattacharyya, A., El-Danaf, E., Kalidindi, S.R., Doherty, R.D., 2001. Evolution of grain-scale microstructure during large strain simple compression of polycrystalline aluminum with quasi-columnar grains: Oim measurements and numerical simulations. International Journal of Plasticity 17, 861–883.

Bobylev, S., Mukherjee, A., Ovid'ko, I., Sheinerman, A., 2010. Effects of intergrain sliding on crack growth in nanocrystalline materials. International Journal of Plasticity 26, 1629–1644.

Bozek, J., Hochhalter, J., Veilleux, M., Liu, M., Heber, G., Sintay, S., Rollett, A., Littlewood, D., Maniatty, A., Weiland, H., et al., 2008. A geometric approach to modeling microstructurally small fatigue crack formation: I. probabilistic simulation of constituent particle cracking in aa 7075-t651. Modelling and Simulation in Materials Science and Engineering 16, 065007.

Brahme, A.P., Inal, K., Mishra, R.K., Saimoto, S., 2011. The backstress effect of evolving deformation boundaries in fcc polycrystals. International Journal of Plasticity 27, 1252–1266.

Brückner-Foit, A., Huang, X., 2006. Numerical simulation of micro-crack initiation of martensitic steel under fatigue loading. International journal of fatigue 28, 963–971.

Cheong, K.S., Busso, E.P., 2004. Discrete dislocation density modelling of single phase fcc polycrystal aggregates. Acta materialia 52, 5665–5675.

Cheong, K.S., Smillie, M.J., Knowles, D.M., 2007. Predicting fatigue crack initiation through image-based micromechanical modeling. Acta materialia 55, 1757–1768.

Choi, S.H., Kim, E.Y., Woo, W., Han, S., Kwak, J., 2013. The effect of crystallographic orientation on the micromechanical deformation and failure behaviors of dp980 steel during uniaxial tension. International Journal of Plasticity 45, 85–102.

Christ, H., Dueber, O., Fritzen, C., Knobbe, H., Koester, P., Krupp, U., Kuenkler, B., 2009. Propagation behaviour of microstructural short fatigue cracks in the high-cycle fatigue regime. Computational Materials Science 46, 561–565.

Dai, H., Parks, D., 1997. Geometrically-necessary dislocation density and scale-dependent crystal plasticity. Khan, A., (Ed.),Proceedings of Sixth International Symposium on Plasticity, Gordon and breach 1, 17–18.

Dunne, F., Wilkinson, A., Allen, R., 2007. Experimental and computational studies of low cycle fatigue crack nucleation in a polycrystal. International Journal of Plasticity 23, 273–295.

Efthymiadis, P., 2015. Multiscale experimentation & modeling of fatigue crack development in aluminium alloy 2024. Ph.D. thesis. University of Sheffield.

Findley, K.O., 2005. Physically-based models for elevated temperature low cycle fatigue crack initiation and growth in Rene 88DT. Ph.D. thesis. Georgia Institute of Technology.

Fine, M.E., Bhat, S.P., 2007. A model of fatigue crack nucleation in single crystal iron and copper. Materials Science and Engineering: A 468, 64–69.

Ghadbeigi, H., Pinna, C., Celotto, S., 2012. Quantitative strain analysis of the large deformation at the scale of microstructure: comparison between digital image correlation and microgrid techniques. Experimental mechanics 52, 1483–1492.

Hochhalter, J., Littlewood, D., Christ Jr, R., Veilleux, M., Bozek, J., Ingraffea, A., Maniatty, A., 2010. A geometric approach to modeling microstructurally small fatigue crack formation: Ii. physically based modeling of microstructure-dependent slip localization and actuation of the crack nucleation mechanism in aa 7075-t651. Modelling and Simulation in Materials Science and Engineering 18, 045004.

Hochhalter, J., Littlewood, D., Veilleux, M., Bozek, J., Maniatty, A., Rollett, A., Ingraffea, A., 2011. A geometric approach to modeling microstruc-

turally small fatigue crack formation: Iii. development of a semi-empirical model for nucleation. Modelling and Simulation in Materials Science and Engineering 19, 035008.

Hoshide, T., Kusuura, K., 1998. Life prediction by simulation of crack growth in notched components with different microstructures and under multiaxial fatigue. Fatigue & Fracture of Engineering Materials & Structures 21, 201–213.

Huang, X., Brückner-Foit, A., Besel, M., Motoyashiki, Y., 2007. Simplified three-dimensional model for fatigue crack initiation. Engineering Fracture Mechanics 74, 2981–2991.

Jablonski, D., 1981. The effect of ceramic inclusions on the low cycle fatigue life of low carbon astroloy subjected to hot isostatic pressing. Materials science and engineering 48, 189–198.

Kalidindi, S.R., Bronkhorst, C.A., Anand, L., 1992. Crystallographic texture evolution in bulk deformation processing of fcc metals. Journal of the Mechanics and Physics of Solids 40, 537–569.

Kartal, M., Cuddihy, M., Dunne, F., 2014. Effects of crystallographic orientation and grain morphology on crack tip stress state and plasticity. International Journal of Fatigue 61, 46–58.

Kozaczek, K., Petrovic, B., Ruud, C., Kurtz, S., McIlree, A., 1995. Microstructural modelling of grain-boundary stresses in alloy 600. Journal of materials science 30, 2390–2400.

Kuhlmann-Wilsdorf, D., 1999. The theory of dislocation-based crystal plasticity. Philosophical Magazine A 79, 955–1008.

Lee, E., 1969. Elastic-plastic deformation at finite strains. J Appl. Mech. 36, 1–6.

Li, L., Shen, L., Proust, G., 2015. Fatigue crack initiation life prediction for aluminium alloy 7075 using crystal plasticity finite element simulations. Mechanics of Materials 81, 84–93.

Li, Y., Aubin, V., Rey, C., Bompard, P., 2012. Polycrystalline numerical simulation of variable amplitude loading effects on cyclic plasticity and microcrack initiation in austenitic steel 304l. International Journal of Fatigue 42, 71–81.

Luo, C., 2011. Multiscale Modeling & Virtual Sensing for Structural Health Monitoring. Ph.D. thesis. Arizona State University.

Luo, C., Chattopadhyay, A., 2011. Prediction of fatigue crack initial stage based on a multiscale damage criterion. International Journal of Fatigue 33, 403–413.

Ma, A., Hartmaier, A., 2014. On the influence of isotropic and kinematic hardening caused by strain gradients on the deformation behaviour of polycrystals. Philosophical Magazine 94, 125–140.

Manonukul, A., Dunne, F., 2004. High–and low–cycle fatigue crack initiation using polycrystal plasticity, in: Proceedings of the Royal Society of London A: Mathematical, Physical and Engineering Sciences, The Royal Society. pp. 1881–1903.

Manonukul, A., Dunne, F., Knowles, D., Williams, S., 2005. Multiaxial creep and cyclic plasticity in nickel-base superalloy c263. International journal of plasticity 21, 1–20.

Mura, T., Nakasone, Y., 1990. A theory of fatigue crack initiation in solids. Journal of Applied Mechanics 57, 1–6.

Navarro, C., Vázquez, J., Domínguez, J., 2014. 3d vs. 2d fatigue crack initiation and propagation in notched plates. International Journal of Fatigue 58, 40–46.

Nye, J., 1953. Some geometrical relations in dislocated crystals. Acta Metall. 1, 153–162.

Olfe, J., Zimmermann, A., Rie, K., 2000. Simulation of microcrack formation and growth during cyclic loading considering microstructure. INIS Repository 32, 186.

Przybyla, C.P., McDowell, D.L., 2010. Microstructure-sensitive extreme value probabilities for high cycle fatigue of ni-base superalloy in100. International Journal of Plasticity 26, 372–394.

Repetto, E., Ortiz, M., 1997. A micromechanical model of cyclic deformation and fatigue-crack nucleation in fcc single crystals. Acta materialia 45, 2577–2595.

Robert, C., Saintier, N., Palin-Luc, T., Morel, F., 2012. Micro-mechanical modelling of high cycle fatigue behaviour of metals under multiaxial loads. Mechanics of Materials 55, 112–129.

Sangid, M.D., Maier, H.J., Sehitoglu, H., 2011. The role of grain boundaries on fatigue crack initiation–an energy approach. International Journal of Plasticity 27, 801–821.

Shenoy, M., Zhang, J., McDowell, D., 2007. Estimating fatigue sensitivity to polycrystalline ni-base superalloy microstructures using a computational approach. Fatigue & Fracture of Engineering Materials & Structures 30, 889–904.

St-Pierre, L., Héripré, E., Dexet, M., Crépin, J., Bertolino, G., Bilger, N., 2008. 3d simulations of microstructure and comparison with experimental microstructure coming from oim analysis. International Journal of Plasticity 24, 1516–1532.

Sweeney, C., Vorster, W., Leen, S., Sakurada, E., McHugh, P., Dunne, F., 2013. The role of elastic anisotropy, length scale and crystallographic slip in fatigue crack nucleation. Journal of the Mechanics and Physics of Solids 61, 1224–1240.

Tanaka, K., Mura, T., 1981. A dislocation model for fatigue crack initiation. Journal of Applied Mechanics 48, 97–103.

Tsutsumi, S., Toyosada, M., Dunne, F., 2010. Phenomenological cyclic plasticity model for high cycle fatigue. Procedia Engineering 2, 139–146.

Weiland, H., Becker, R., 1999. Analysis of mesoscale deformation structures in aluminum, in: Proceedings of 20th Risø Int. Symp. on Mater. Sci. Deformation-Induced Microstructures: Analysis and Relation to Properties, p. 213.

Xie, C., Fang, Q., Liu, X., Guo, P., Chen, J., Zhang, M., Liu, Y., Rolfe, B., Li, L., 2016. Theoretical study on the deformation twinning and cracking in coarse-grained magnesium alloys. International Journal of Plasticity 82, 44–61.

Zhang, H., Diehl, M., Roters, F., Raabe, D., 2016. A virtual laboratory using high resolution crystal plasticity simulations to determine the initial yield surface for sheet metal forming operations. International Journal of Plasticity 80, 111–138.

Zhang, J., Jiang, Y., 2006. Fatigue of polycrystalline copper with different grain sizes and texture. International Journal of plasticity 22, 536–556.